Skillful long-lead seasonal predictions in the summertime Northern Hemisphere middle latitudes

Hai Lin[1]*, Ryan Muncaster[1], Jacques Derome[2], William J. Merryfield[3], Gulilat Diro[4]

[1] Recherche en prévision numérique atmosphérique, Environment and Climate Change Canada, Montreal, Canada

[2] Department of Atmospheric and Oceanic Sciences, McGill University, Montreal, Canada

[3] Canadian Centre for Climate Modelling and Analysis, Environment and Climate Change Canada, Victoria, Canada

[4] Canadian Centre for Meteorological and Environmental Prediction, Environment and Climate Change Canada, Montreal, Canada

Corresponding author address:

Hai Lin, Recherche en prévision numérique atmosphérique, Environment and Climate Change Canada, 2121 Trans-Canada Highway, Dorval, Québec H9B 1J3. Email: hai.lin@ec.gc.ca

Abstract

In contrast to boreal winter when extratropical seasonal predictions benefit greatly from ENSO-related teleconnections, our understanding of forecast skill and sources of predictability in summer is limited. Based on 40 years of hindcasts of the Canadian Seasonal to Inter-annual Prediction System version 3 (CanSIPSv3), this study shows that predictions for the Northern Hemisphere summer are skillful more than six months in advance in several middle latitude regions, including eastern Europe−Middle East, central Siberia−Mongolia−North China, and the western United States. These midlatitude regions of statistically significant predictive skill appear to be connected to each other through an upper tropospheric circum-global wave train. Although a large part of the forecast skill for the surface air temperature and 500 hPa geopotential height is attributable to the linear trend associated with global warming, there is significant long-lead seasonal forecast skill related to interannual variability. Two additional idealized hindcast experiments are performed to help shed light on sources of the long-lead forecast skill using one of the CanSIPSv3 models and its uncoupled version. It is found that tropical ENSO related SST anomalies contribute to the forecast skill in the western United States, while land surface conditions in winter, including snow cover and soil moisture, in the Siberian and western United States regions have a delayed or long-lasting impact on the atmosphere, which leads to summer forecast skill in these regions. This implies that improving land surface initial conditions and model representation of land surface processes is crucial for further development of a seasonal forecasting system.

Significance Statement

Useful seasonal predictions in the boreal summer middle latitude regions are of great value. In this study, we show that predictions for the boreal summer season are skillful more than six months in advance in several middle latitude regions, including eastern Europe−Middle East, central Siberia−Mongolia−North China, and the western United States. The forecast skill in these regions is associated with a circum-global teleconnection atmospheric circulation pattern. Sources of the long-lead forecast skill include the global warming related trend and anomalies in the ocean and land surface initial conditions. It is found that the wintertime snow cover and soil moisture in the Siberian and western United States regions have a delayed or long-lasting impact on the atmosphere, which leads to summer forecast skill.

1. Introduction

Dynamical seasonal predictions are routinely produced at many operational meteorological centers. Unlike numerical weather predictions that depend primarily on accurate description of atmospheric initial conditions, seasonal forecasts benefit from atmospheric interactions with more slowly varying climate system components, e.g., ocean, sea ice, and land surface. The El Nino – Southern Oscillation (ENSO) phenomenon has long been identified as the most important source of predictability for seasonal predictions (e.g., Shukla et al. 2000; Derome et al. 2001; Yeh et al. 2018; Weisheimer et al. 2020). Changes of diabatic heating in the tropical Pacific associated with sea surface temperature (SST) anomalies of ENSO induce large-scale Rossby waves propagating into the middle and high latitudes, influencing the extratropical weather. Significant atmospheric response to ENSO and other forcing is usually found in the winter season in the Northern Hemisphere when the subtropical westerly jet is strong. For this reason, most previous seasonal prediction and predictability studies focused on the winter season (e.g., Kim et al., 2012; Scaife et al. 2014; Johnson et al. 2014; Butler et al. 2016). For example, ENSO is associated with the wintertime Pacific-North American (PNA) teleconnection pattern (e.g., Wallace and Gutzler 1981), which is likely responsible for the forecast skill of December-January-February (DJF) 500-hPa geopotential height in that region (e.g., Shukla et al. 2000; Derome et al. 2001; Lin et al. 2020; Weisheimer et al. 2020).

Less is known about the seasonal forecast skill and sources of predictability in the extratropical regions in the boreal summer season than winter. This does not mean that a forecast for the summer season is not as important. As a matter of fact, a useful seasonal prediction for the summer season is of great value to the public, and to many sectors such as agriculture, health, and energy, especially in the Northern Hemisphere middle latitude regions where the population is large. Summertime heatwaves make significant societal impacts (e.g., Changnon et al. 1996; Lin et al. 2022), and are becoming more frequent with global warming (e.g., Seneviratne et al.

2012). The probability and frequency of heatwaves are closely associated with summertime seasonal mean surface air temperature (e.g., Jia et al. 2022).

In this study, we examine the summertime seasonal forecast skill in the Northern Hemisphere middle latitudes at lead times ranging from zero to nine months. Analysis is performed using the 40-year hindcast output data from two global coupled models of the Canadian Seasonal to Interannual Prediction System version 3 (CanSIPSv3) which is being implemented in operations in early summer 2024. We show that seasonal forecasts for the boreal summer season are skillful in several middle latitude land regions a few months in advance. We explain the long-lead forecast skill and explore sources of predictability through idealized hindcast experiments.

Section 2 describes the CanSIPSv3 models and data that we use in this study. Section 3 presents the forecast skill in the boreal summer. Section 4 presents the forecast skill for the hindcast with trends removed, so that contributions from trends and interannual variability are assessed. In section 5, how the forecast skills in different middle latitude regions are connected to each other and to circulation patterns are analyzed. In section 6, sources of the long-lead summer time seasonal forecast skill and predictability are explored by performing two idealized hindcast experiments. A summary and discussion are given in Section 7.

2. Models and data

CanSIPSv3 is the third version of the Canadian Seasonal to Interannual Prediction System, which is recently developed for Innovation Cycle phase 4 (IC-4) of the Canadian Centre for Meteorological and Environmental Prediction (CCMEP) of Environment and Climate Change Canada (ECCC) and is being implemented in operations in early summer 2024. Like CanSIPSv2 (Lin et al. 2020), CanSIPSv3 consists of two global coupled models, GEM5.2-NEMO and CanESM5.1, and thus is a multi-model ensemble system. With each model, 20-member hindcasts of 40 years (1981-2020) are made starting from the beginning of each month with a range of 12 months. Of the 20 ensemble members, 10 are initialized on the 1st of the month and the other 10 five days before. For example, for the hindcast of January 1, 2000, 10 members are initialized at 00Z January 1, 2000, and 10 members start at 00Z December 27, 1999. GEM5.2-NEMO is an upgraded version of GEM-NEMO in CanSIPSv2 and GEM5.1-NEMO in CanSIPSv2.1, which are described in detail in Lin et al. (2020; 2021) and Sospedra-Alfonso et al. (2024). Its most basic features and major changes are outlined below. CanCM4i in CanSIPSv2.1 is replaced by CanESM5.1 in CanSIPSv3.

a. GEM5.2-NEMO

Developed at Recherche en Prévision Numérique (RPN), GEM5.2-NEMO is a fully coupled global model. Its atmospheric component is the Global Environmental Multiscale (GEM) model (Côté et al. 1998; Girard et al. 2014), which is the operational Numerical Weather Prediction (NWP) model at ECCC. The GEM version 5.2 in CanSIPSv3 has a Yin-Yang grid and is configured with a horizontal resolution of 1 degree and 85 vertical levels. For the land surface module, the ISBA scheme (Noilhan and Planton 1989; Noilhan and Mahfouf 1996) is applied. Soil moisture is represented in two layers with a 10 cm upper layer and a location dependent deep layer.

The ocean component is NEMOv3.6 on the ORCA1 grid with a nominal horizontal resolution of 1° × 1° (1/3° meridionally near the equator) and 50 vertical levels. The CICE 6.0 model is used for the sea ice component with five ice-thickness categories.

In the hindcast, the atmospheric initial conditions are based on the European Centre for Medium-Range Weather Forecasts (ECMWF) reanalysis version 5 (ERA5; Hersbach et al. 2020). Random isotropic perturbations are added to the reanalysis fields to create initial conditions for different ensemble members with a similar method to that in the ECCC monthly forecast system (Lin et al. 2016). The ORAS5 reanalysis (Zuo et al. 2015) is used to initialize the 3-D ocean temperature, salinity, and currents, as well as sea surface height and sea ice thickness. The sea ice concentration is initialized with Had2CIS (Lin et al. 2020), which consists of HadISST2.2 (Titchner and Rayner 2014) combined with the Canadian Ice Service data (Tivy et al. 2011). The land surface initial conditions in the hindcast come from an offline historical run of the Surface Prediction System (SPS), which is the same ISBA surface scheme as in the GEM model (Carrera et al. 2010), forced by the near-surface atmospheric and the precipitation fields of the ERA5 reanalysis. The greenhouse gas (GHG) concentrations are prescribed for each hindcast year as observed annual globally averaged values that are assembled at RPN from several sources including the World Meteorological Organization Greenhouse Gas Bulletin (https://wmo.int/publication-series/greenhouse-gas-bulletin).

b. CanESM5.1

CanESM5.1 derives from the Canadian Earth System Model version 5 (Swart et al. 2019) in the form of the p1 variant described in Sigmond et al. (2023), which is a fully coupled ocean-atmosphere-land-sea ice climate model developed at the Canadian Centre for Climate Modelling and Analysis (CCCma). The atmospheric component has a horizontal T63 spectral resolution (approximately 2.8°) with 49 hybrid vertical coordinate levels. CanESM5.1 employs version 3.6.2 of the Canadian Land Surface Scheme (CLASS; Verseghy 2000) and the Canadian Terrestrial Ecosystem Model (CTEM).

The ocean component is NEMOv3.4.1 on the ORCA1 grid with a nominal horizontal resolution of 1° × 1° (1/3° meridionally near the equator) and 45 vertical levels. The LIM2 model (Fichefet and Morales Maqueda 1997) is used for the sea ice component.

In the hindcast, the initial conditions of atmosphere, ocean, land, and sea ice come from assimilation coupled runs with the atmosphere, ocean and sea ice concentration nudged to the ERA5 and ORAS5 reanalysis, and Had2CIS, respectively, and the sea ice thickness constrained to values derived from the SMv3 statistical model of Dirkson et al. (2017). A set of parallel assimilation runs starting from different dates are performed to generate initial conditions for different ensemble members. The GHG concentrations are prescribed in the hindcast as the CMIP6 historical (omitting volcanic forcing from eruptions that occur after initialization) and the SSP2-45 scenarios.

A novel aspect of the CanESM5.1 hindcasts is the introduction of tendency correction terms in the prognostic equations for atmospheric wind, temperature, and humidity, together with ocean temperature and salinity. These cyclostationary corrections are derived as described in Kharin and Scinocca (2012) from nudging runs similar to those that provide the initial conditions, but with nudging coefficients adjusted to minimize biases in runs with the tendency corrections applied. This generally reduces climatological biases in the hindcasts, and generally improves their skill.

c. Verification data and analysis methods

We use ERA5 reanalysis as the verification and analysis data, which include monthly mean 2-m temperature (T2m), 500-hPa and 200-hPa geopotential height (Z500 and Z200), precipitation rate (PR), and sea surface temperature (SST). For simplicity, hereafter the reanalysis data are referred to as observations. Both the observation and model data are interpolated into a 2.5° ×2.5° resolution before the analysis.

As a measure for deterministic seasonal forecast skill, we use temporal anomaly correlation coefficient (ACC) between the seasonally averaged observational and ensemble mean forecast anomalies over the 40 years of hindcast. A Student's *t* test is used to assess the statistical significance for the grid-point ACC skill. The effective number of degrees of freedom is reduced by the autocorrelation of the time series as estimated according to Bretherton et al. (1999).

The Continuous Ranked Probabilistic Skill Score (CRPSS; e.g., Bradley and Schwartz 2011; Wilks 2011) is calculated as probability skill of the ensemble seasonal forecast. CRPSS measures the fractional improvement in error of the forecast distribution relative to a forecast based on the observed climatology. Here it is calculated following the methodology as described in Kharin et al. (2017). The statistical significance of CRPSS is obtained based on a bootstrapping resampling method.

d. Idealized hindcast experiments

To explore sources of predictability and explain the long-lead seasonal forecast skill in the summertime Northern Hemisphere middle latitudes, two idealized hindcast experiments are performed, both initialized at the beginning of February. As in the hindcast, each experiment produces 12-month integrations of 20 members over 40 years of 1981-2020.

In the first experiment (Exp 1), GEM5.2-NEMO, one of the coupled models in CanSIPSv3, is used. The objective of this experiment is to study the contribution of ocean and sea ice initial conditions. Therefore, realistic ocean and sea ice initial conditions that are the same as in the GEM5.2-NEMO hindcast are utilized. For the atmosphere and land, however, the forecasts of 39 years, from 1981 to 2020 excluding 1991, start from the February 1991 initial condition, which is that of February 1, 1991, for 10 members and January 27, 1991, for the other 10 members. For the 1991 forecast, the initial conditions of February 1990 are used. In this way, there would be no contribution to the forecast skill from atmosphere and land initial conditions. The forecast skill would mainly come from the initial conditions of the ocean and sea ice.

In the second experiment (Exp 2), we aim to isolate the contribution of land surface conditions at the beginning of February to the forecast skill of Northern Hemisphere middle latitudes in summer, by excluding the impact of ocean and sea ice. For this purpose, we use the uncoupled atmospheric model, GEM5.2, which is the atmospheric component of GEM5.2-NEMO. The initial conditions for the atmosphere and land are realistic, which are the same as in the GEM5.2-NEMO hindcast, but the initial SST and sea ice concentration are quickly (in 15 days) relaxed to prescribed climatological SST and sea ice concentration. Therefore, seasonal forecast skill with several month lead time, if any, would mainly come from land surface initial conditions. While there is interannual variability in the atmospheric initial conditions, its influence can be expected to vanish over a period of a few weeks, with any longer-term influences such as from the Quasi-Biennial Oscillation expected to be minor.

Atmospheric trends over the 40 years of hindcast may come from trends in the initial conditions and be generated in the model integration because of changes in the specified GHG concentrations. In the case of Exp 1, trends are introduced from the ocean and sea ice initial conditions and are generated by radiative forcing of the specified yearly GHG concentrations. In Exp 2, we use constant GHG concentrations (e.g., 380 ppm of CO_2) for all the 40 years, so that the main source of trends in the summertime seasonal means in this experiment would be the land surface initial condition.

3. Seasonal mean forecast skill of JJA

We start by looking at the forecast skill of JJA seasonal mean T2m for the hindcasts at different lead times. Shown in Fig. 1 is the anomaly correlation skill of ensemble mean forecasts for JJA T2m by the two CanSIPSv3 models over the Northern Hemisphere land at lead times of one (initialized on May 1) to four (initialized on February 1) months. Significant forecast skill is seen in the middle latitudes, with high values mainly in three regions: eastern Europe and Middle East; Siberia-Mongolia-North China; and the western United States. Relatively larger positive correlations are also found near eastern Canada. It is interesting that the skill distribution and strength are almost independent of lead time. Skillful T2m seasonal predictions are obtained for the summertime Northern Hemisphere middle latitudes several months in advance. The two CanSIPSv3 models have very similar behavior and performance, indicating that the long lead forecast skill is not model dependent but likely determined by the fundamental nature of the climate system. When the ensemble forecasts of the two CanSIPSv3 models are combined, the skill is enhanced with a similar distribution (Fig. S1), consistent with previous studies showing that a multi-model forecast outperforms individual models (e.g., Krishnamurti et al. 1999; Kharin et al. 2009; Becker et al. 2014).

Not only does the ensemble mean deterministic forecast show long-lead skill, but similar results are also obtained from the CRPSS skill of probabilistic forecasts (Fig. 2).

Based on the Geophysical Fluid Dynamics Laboratory (GFDL) SPEAR seasonal prediction system, Jia et al. (2022) reported that the seasonal prediction of North American summertime heat extremes is skillful several months in advance. A similar result of long lead forecast skill of JJA T2m in the western United States presented here was found in their study. This indicates that common sources of skill for the summer T2m forecast in that region are captured in all the CanSIPSv3 and SPEAR models.

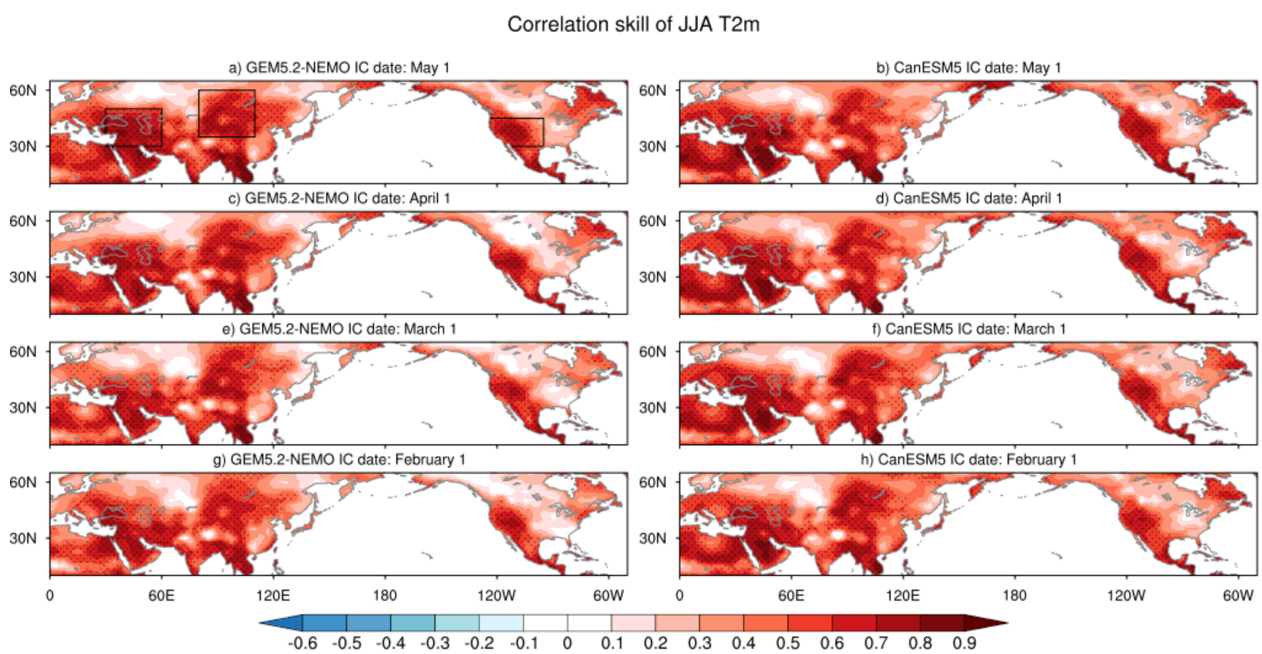

Figure 1 Correlation between the observed seasonal mean T2m anomaly and its ensemble mean forecast for the target season of JJA over the Northern Hemisphere land obtained from 40-year hindcasts of GEM5.2-NEMO (left) and CanESM5.1 (right). The hindcasts are initialized on (a and b) May 1, (c and d) April 1, (e and f) March 1, and (g and h) February 1. Stippling indicates that the correlation is statistically significant at the 0.05 level based on a Student's *t* test. The dark-lined boxes in (a) outline the three regions that will be further analyzed and discussed.

For the forecast of JJA seasonal mean precipitation rate (Fig. 3), the anomaly correlation skill is weaker than that of T2m. However, comparing to Fig. 1, we do see relatively high PR forecast skill over the regions where the T2m skill is high at a lead time of one to four months, and the two

CanSIPSv3 models agree with each other. Therefore, there is also appreciable long-lead forecast skill for JJA seasonal mean precipitation in the middle latitudes.

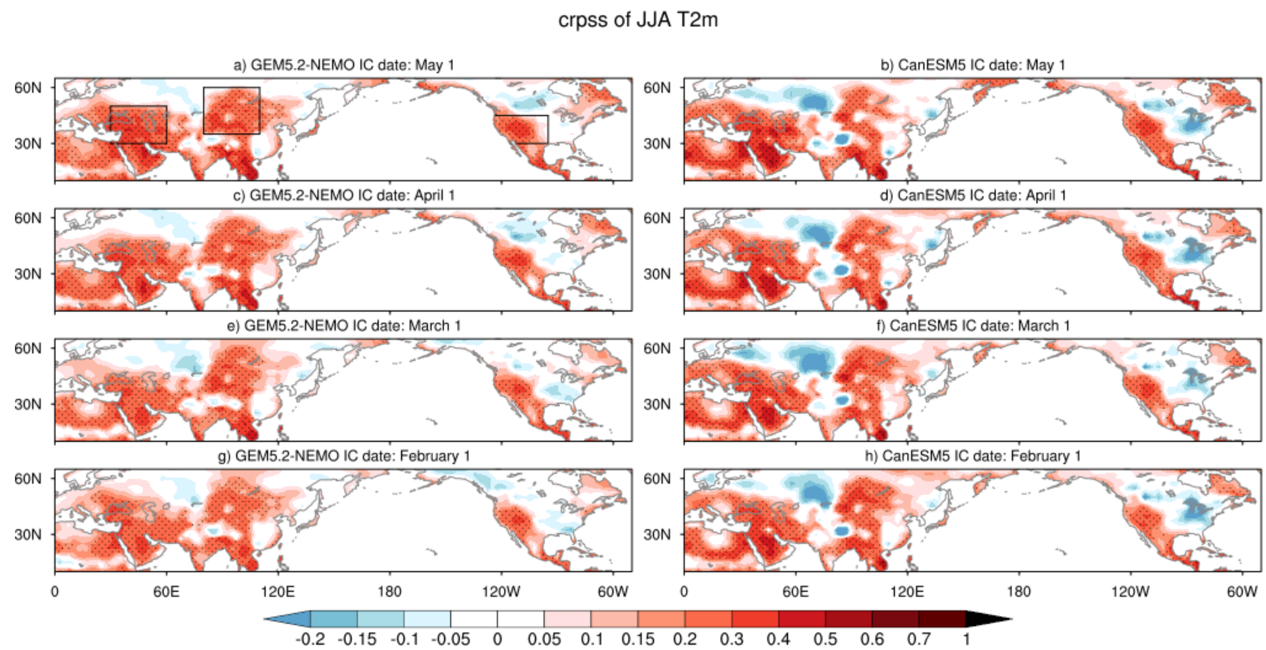

Figure 2 Same as Fig. 1, but for CRPSS. Stippling indicates that the CRPSS is significantly greater than 0 at the 0.05 level based on a bootstrapping resampling method.

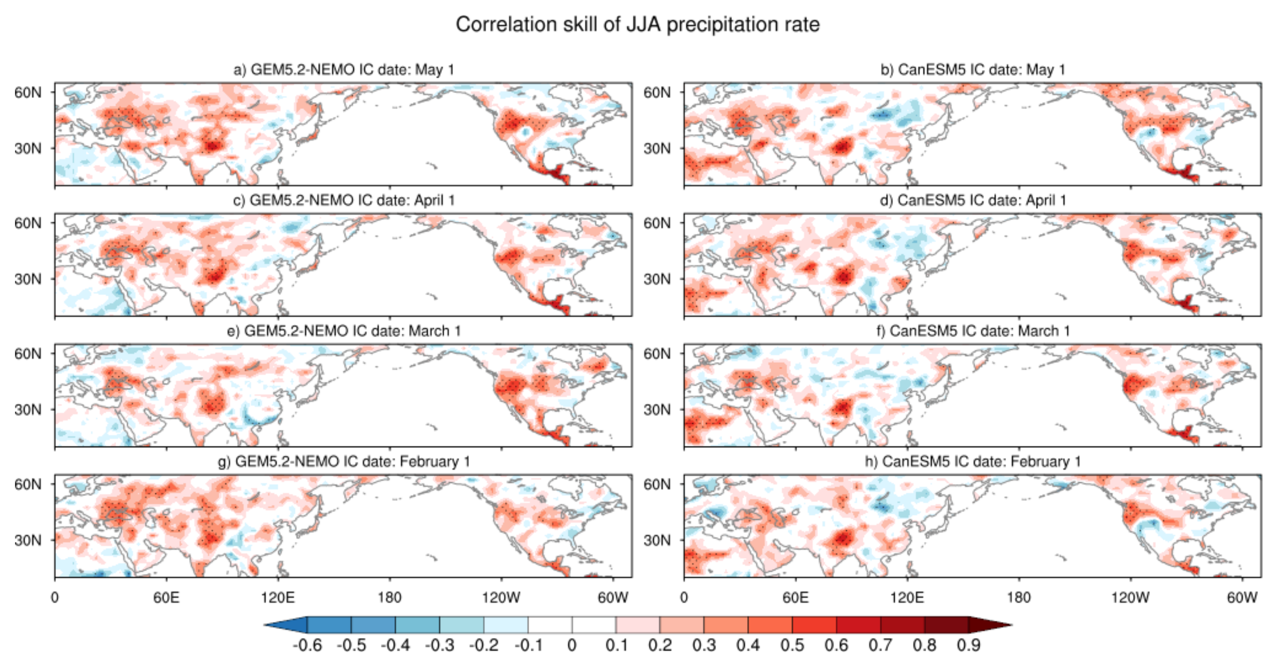

Figure 3 Same as Fig. 1, but for JJA precipitation rate.

The anomaly correlation skill of JJA Z500 by the CanSIPSv3 models is presented in Fig. 4 over the Northern Hemisphere. Again, the forecast is skillful at a long lead time and the two models behave similarly. In the middle latitudes, there appear to exist five centers of higher skill values that tend to form a wave train around the globe. In addition to the three centers over the continents that correspond to the T2m skill, two oceanic centers can be found, one over the North Pacific and the other over the western North Atlantic. Similar wave-train like JJA Z500 skill distribution was observed in CanSIPSv2 for the 1-month lead forecast (Lin et al. 2020). It is likely that the zonal distribution of summertime middle latitude forecast skill is associated with a circum-global teleconnection pattern (CGT; e.g., Branstator 2002; Ding and Wang 2005; Beverly et al. 2019). We will come back to this point in section 5.

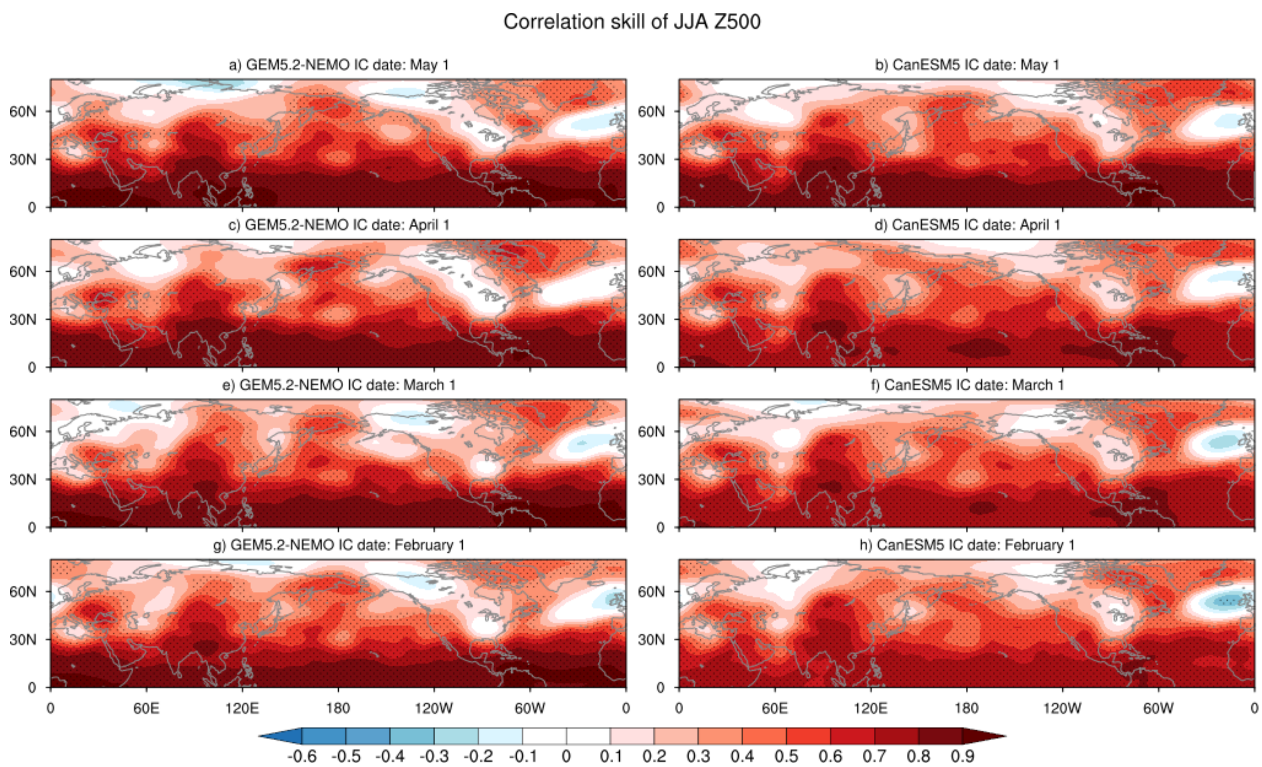

Figure 4 Correlation between the observed seasonal mean Z500 anomaly and its ensemble mean forecast for the target season of JJA over the Northern Hemisphere obtained from 40-year hindcasts of GEM5.2-NEMO (left) and CanESM5.1 (right). The hindcasts are initialized on (a and b) May 1, (c and d) April 1, (e and f) March 1, and (g and h) February 1. Stippling indicates that the correlation is statistically significant at the 0.05 level based on a Student's *t* test.

In the above discussions, the spatial distribution of JJA skill is presented for the forecasts at lead times of one to four months. To understand the dependence of forecast skill on lead time and season in the Northern Hemisphere middle latitudes, three midlatitude regions of higher forecast skill of JJA T2m are selected as outlined by the dark-lined boxes in Fig. 1a. They are Region 1: eastern Europe and Middle East, 30°-60°E, 30°-50°N; Region 2: Siberia-Mongolia-North China, 80°-110°E, 35°-60°N; Region 3: western United States, 125°-95°W, 30°-45°N. Anomaly correlation skill of seasonal mean (three-month average) T2m is averaged over the land grid cells of each region for all the lead times and all seasons with the 40-year hindcasts initialized every month. Figure 5 provides a summary of the area-averaged correlation skill of the seasonal mean T2m for the two CanSIPSv3 models, which shows the area-averaged anomaly correlation skill as a function of lead time and target season for each region. As can be seen, for all three regions, the T2m forecast skill tends to peak around the summer seasons. Statistically significant forecast skill for the summer seasons (e.g., JJA and JAS) is obtained for all lead times from zero to nine months, the maximum lead time for a 12 month seasonal forecast. For the target season of JJA, for example, the nine-month lead forecast starts from September 1 of the previous year. Therefore, in these midlatitude regions, summertime seasonal mean T2m anomalies can be predicted with higher skill more than half a year in advance. The same conclusion can be made with the area averaged CRPSS of the seasonal mean T2m (Fig. S2).

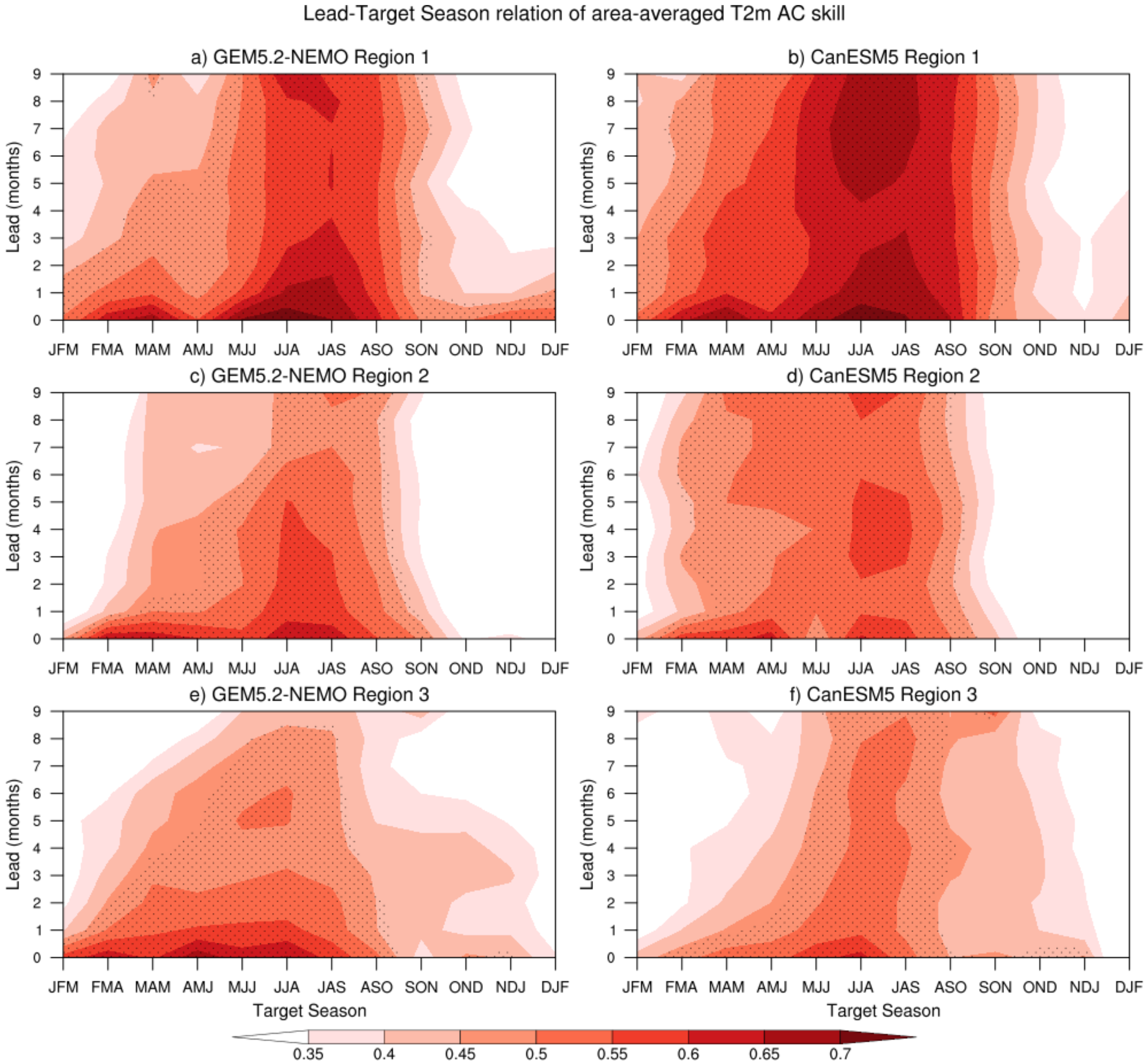

Figure 5 Area averaged anomaly correlation skill of seasonal mean T2m as a function of target season (horizontal axis) and lead time (vertical axis). Left panels are for GEM5.2-NEMO, and right panels for CanESM5.1. (a) and (b) are for area averaged correlation in Region 1, (c) and (d) in Region 2, and (e) and (f) in Region 3. Stippling indicates that the area-averaged correlation is significantly greater than 0.3 at the 0.05 level based on a bootstrapping resampling method.

4. Contribution of trends and interannual variability

Trends related to climate change influence seasonal forecast skill. Trends were shown to be among the most important predictors in statistical predictions of monthly and seasonal temperatures in North America (e.g., Peng et al. 2012; Johnson et al. 2014). In dynamical seasonal predictions, trends are introduced through initial conditions of the atmosphere, land, ocean, and sea ice, and can be generated by radiative forcing of greenhouse gases in the model. Seasonal forecast skill in general benefits from a realistic representation of trends (e.g., Doblas-Reyes *et al.*, 2006; Liniger *et al.*, 2007; Boer, 2009). Trends tend to be predictable, whereas predicting the interannual variability is more challenging. In this section, we try to identify the part of summertime seasonal forecast skill that arises from the interannual variability and is independent of the trend by detrending the hindcast and verification data.

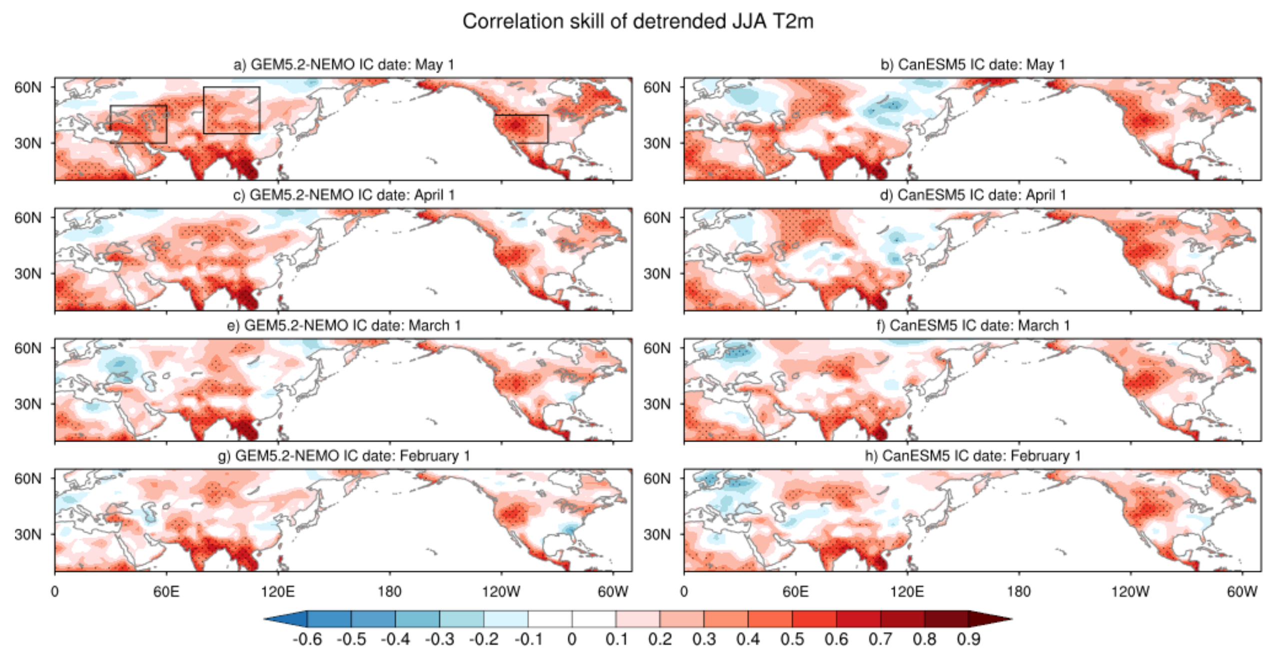

Figure 6 Same as Fig. 1, but for detrended seasonal mean T2m.

The correlation skill calculated for the detrended JJA seasonal mean T2m anomalies is illustrated in Fig. 6. The skill is considerably weaker than when the trend is retained. This indicates that trends contribute to a large part of the JJA seasonal mean T2m skill discussed above, e.g., Figs. 1 and 5. However, there is still statistically significant long lead forecast skill for the JJA T2m in the middle latitudes that is associated with the interannual variability. This is especially clear for the Siberia-Mongolia-North China region (Region 2) and the western US (Region 3), where both CanSIPSv3 models produce skillful predictions at all the lead times from one to four months. On the other hand, in the eastern Europe and Middle East region (Region 1), statistically significant forecast skill of detrended JJA T2m can only be found for the forecasts from May 1 (1-month lead) in both models (Fig. 6a and b), and April 1 (2-month lead) in GEM5.2-NEMO (Fig.

6c). At a longer lead time, there is little forecast skill in Region 1 that is associated with the interannual variability.

The correlation skill of the detrended JJA Z500 anomaly for the two CanSIPSv3 models at lead times from 1 to 4 months is shown in Fig. 7. Two maximum skill centers are seen over the Siberian region and the western United States, corresponding to the T2m skill in Regions 2 and 3, respectively (Fig. 6). Statistically significant skill of detrended summertime Z500 is also found over the North Pacific and western North Atlantic areas, indicating that as in the Siberian and western United States regions there is a significant part of the Z500 skill observed in Fig. 4 over the oceanic regions coming from the interannual variability.

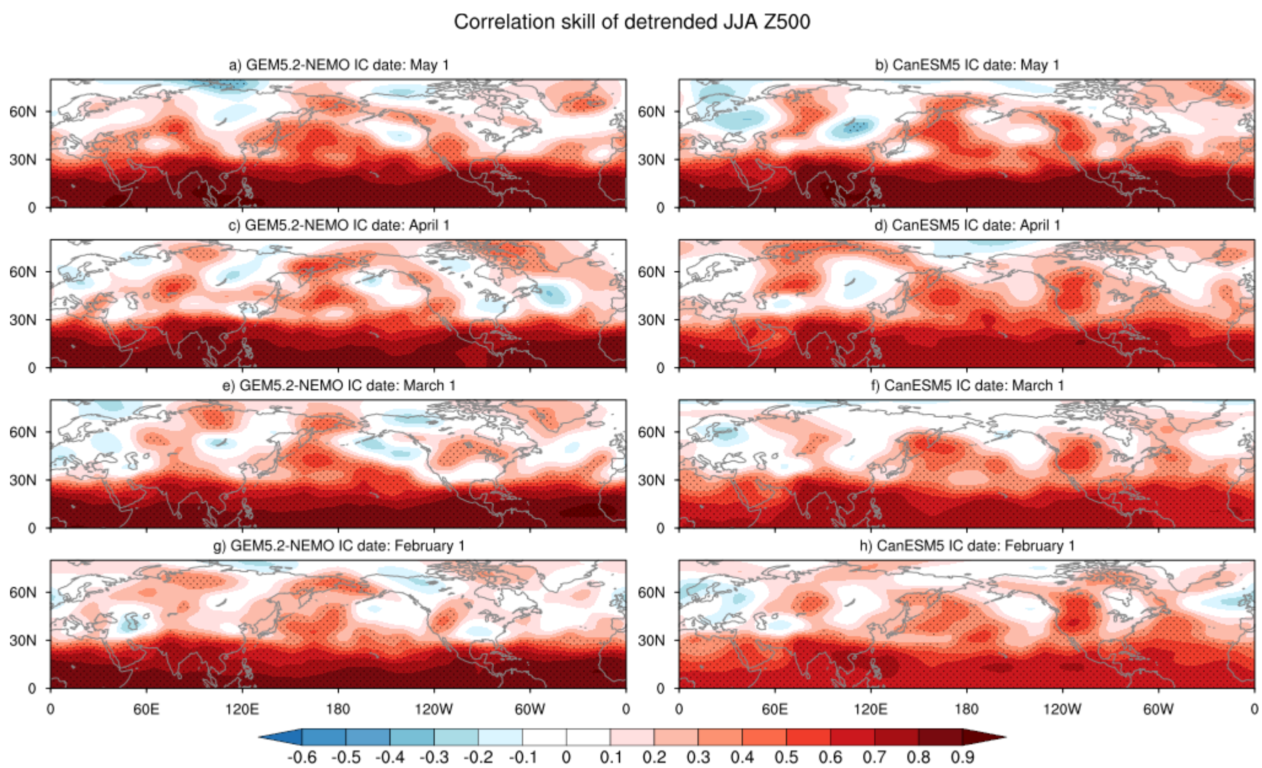

Figure 7 Same as Fig. 4, but for detrended seasonal mean Z500.

As for the correlation skill of detrended JJA precipitation anomaly (Fig. S3), the distribution is similar to that with the trend retained as in Fig. 4. The trend has a small influence on the JJA seasonal mean precipitation forecast in the western United States, where the detrended correlation skill is statistically significant although slightly weaker than that in Fig. 4 for a lead time as long as three months (March 1 start). This indicates that the interannual variability of JJA precipitation in this region is predictable up to three months in advance. Over the Eurasian continent, the detrended forecast skill of JJA precipitation is less well organized and weaker than that including the trend for a forecast more than one month in advance.

In summary, forecast skill of JJA T2m in Region 1 at a lead time longer than two months as observed in Figs. 1 and 5 appears to mainly result from the trend, while that in Regions 2 and 3 includes contributions from both the trend and interannual variability. In Region 3 the interannual variability of summertime T2m, Z500 and precipitation all have a long-lead forecast skill, whereas in Region 2 forecasting the interannual variation part of JJA precipitation anomaly is not skillful at a lead time longer than one month in contrast to T2m and Z500.

5. Link to tropospheric circulation patterns

We have so far demonstrated that the summertime seasonal mean atmospheric condition in three middle latitude land regions can be predicted with some skill several months in advance. In this section, through diagnostic analysis of the ERA5 reanalysis, we investigate how the T2m variability in these three regions is interconnected and associated with the tropospheric circulation.

Figure 8 shows the correlations of area-averaged JJA seasonal mean T2m anomalies in Regions 1, 2 and 3 with the JJA T2m anomalies at every grid point. To assess the contribution of interannual variability, the calculation is repeated with detrended data (right panels). As is evident from Fig. 8, JJA T2m anomalies in the three regions are positively correlated to each other. The correlation is stronger, and the centers are more consistent when trends are retained (Fig. 8 left panels) than when only the interannual variability part is considered (Fig. 8 right panels). As JJA seasonal mean T2m anomalies in these three regions are connected, it is likely that they are a result of the same process. Trends appear to strengthen the connection among the three regions. When only the interannual variability is considered, the correlations between Regions 1 and 2 and between Regions 2 and 3 are statistically significant, but that between Regions 1 and 3 is relatively weak (Table 1).

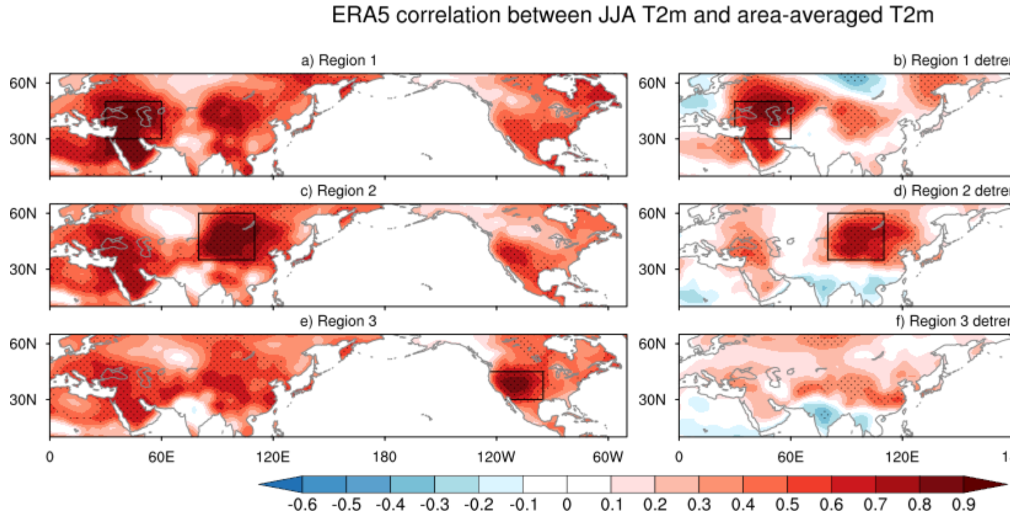

Figure 8 Correlation between area averaged JJA T2m anomalies in (a) Region 1, (c) Region 2, and (e) Region 3 with JJA T2m anomaly at every land grid point based on the ERA5 reanalysis from 1981 to 2020. The panels on the right (b, d and f) are the same as the left but with detrended JJA T2m anomalies. Stippling indicates that the correlation is statistically significant at the 0.05 level based on a Student's *t* test. The dark-lined box in each panel outlines the base region.

	R1-R2	**R1-R3**	**R2-R3**
with trend	**0.78**	**0.69**	**0.74**
detrended	**0.36**	0.30	**0.42**

Table 1 Cross-correlations of the area-averaged JJA T2m anomalies in Regions 1, 2 and 3. Numbers in bold are statistically significant at the 0.05 level based on a Student's *t* test.

To see how the T2m variability in Regions 1, 2 and 3 is associated with the upper tropospheric circulation, area averaged JJA T2m anomalies are correlated with JJA Z200 at every grid point with and without trends (Fig. 9). From the correlation maps, a middle latitude wave train with wavenumber 5 or 6 along the jet stream can be discerned that looks like the observed circum-global teleconnection pattern (e.g., Branstator 2002; Ding and Wang 2005; Ding et al. 2011). The positive centers of the wave train which represent Z200 ridges are located near midlatitude eastern Europe, Siberia, and the western United States, in addition to those over the North Pacific and North Atlantic. With the trend removed (Fig. 9 right panels), the Z200 correlation appears to have the same distribution as that including the trend, but the magnitude is reduced. This indicates that the trend itself has a circum-global teleconnection structure in the upper troposphere that is associated with localized T2m anomalies in the middle latitudes. Teng et al. (2022) demonstrated that indeed the warming trend pattern over the Northern Hemisphere middle latitudes in boreal summer of 1979-2020 is characterized by hot spots in the land regions including Europe, central Siberia and Mongolia, and west coast of North America, which is accompanied by a chain of anomalous high-pressure ridges of an upper tropospheric circum-global Rossby wave train. They suggested that the circulation trend pattern is associated with fluctuations of the Atlantic multi-decadal variability and the interdecadal Pacific oscillation, as well as contribution from interactions with atmospheric synoptic-scale transients.

On the interannual time scale, our analysis shows that the T2m variability in the three analyzed regions is also closely connected to a circum-global wave train which has the same pattern as the trend (Fig. 9 right panels). It is possible that some similar mechanisms are responsible for the generation of the middle-latitude circulation pattern both in the trend and on the interannual time scale. The boreal summer circum-global teleconnection pattern was observed to be related to interannual variability of tropical and extratropical forcing. For example, this pattern was found to be associated with diabatic heating anomalies of the Indian summer monsoon (e.g., Ding and Wang 2005; Lin 2009; Ding et al. 2011), and with land temperature anomalies of the Tibetan Plateau (Xue et al. 2022).

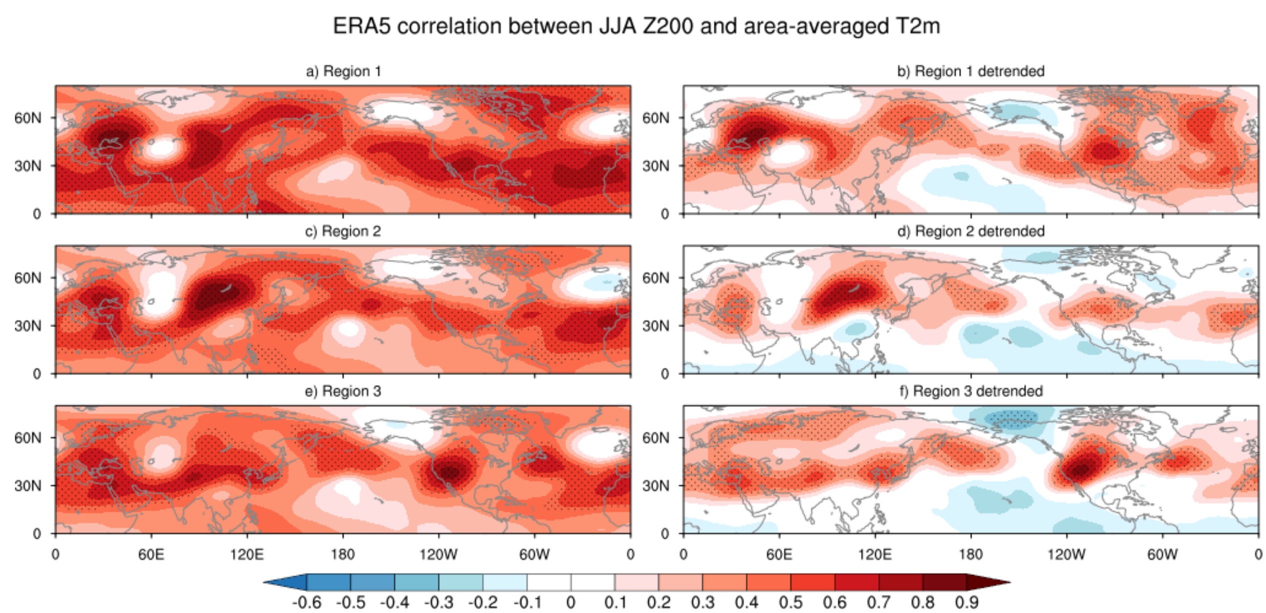

Figure 9 Correlation between area averaged JJA T2m anomalies in (a) Region 1, (c) Region 2, and (e) Region 3 with JJA Z200 anomaly at every land grid point based on the ERA5 reanalysis from 1981 to 2020. The panels

on the right (b, d and f) are the same as the left but with detrended data. Stippling indicates that the correlation is statistically significant at the 0.05 level based on a Student's *t* test.

6. Sources of predictability

In this section, we attempt to explain the long lead forecast skill in the summertime Northern Hemisphere middle latitudes as observed above and explore sources of predictability through idealized hindcast experiments. As described in detail in section 2, two experiments are conducted, Exp 1 with the GEM5.2-NEMO coupled model and Exp 2 with the uncoupled GEM5.2 atmospheric model. The objective is to answer the question of what processes are essential for the model to produce skillful long-lead predictions for the boreal summer season in the middle latitudes.

Shown in Fig. 10a is the anomaly correlation skill of JJA seasonal mean T2m anomaly of Exp 1 at a 4-month lead time. As the atmosphere and land are initialized with conditions different from the current year, the forecast skill mainly comes from the initial conditions of the ocean and sea ice, as well as GHG concentration changes. Statistically significant skill is seen in the Northern Hemisphere middle latitudes, with maximum values in the regions of eastern Europe-Middle East, Siberia-Mongolia-North China, and the western United States. Compared to the GEM5.2-NEMO hindcast initialized on February 1 (Fig. 1g), the skill of Exp 1 has a very similar distribution but weaker in the three regions of interest. The skill due to interannual variability, i.e., the detrended skill (Fig. 10b), is not statistically significant in Region 1, and weaker in Regions 2 and 3 than that of the GEM5.2-NEMO hindcast (Fig. 6g). This indicates that the ocean and sea ice initial conditions contribute to the long-lead summertime forecast skill in the middle latitude regions, but they are not the only contributing factors.

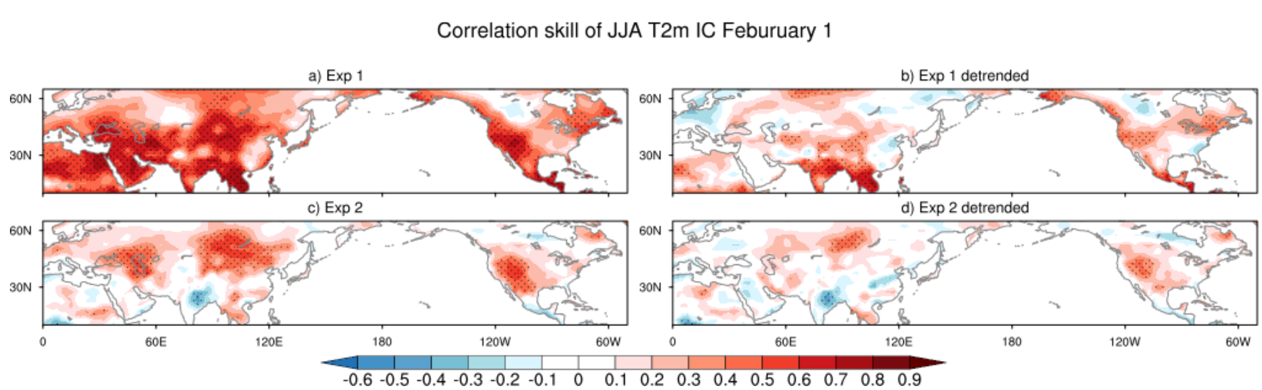

Figure 10 Anomaly correlation skill of JJA seasonal mean T2m of (a) Exp 1 and (b) Exp 2. Both hindcasts are initialized on February 1. (b) and (d) are corresponding correlation skill of detrended T2m. Stippling indicates that the correlation is statistically significant at the 0.05 level based on a Student's *t* test.

Figure 10 (c) and (d) are anomaly correlation skill of JJA T2m of Exp 2 with and without the trend, respectively. As described in section 2, this experiment is conducted using the uncoupled GEM5.2 atmospheric model with specified climatological SST and sea ice concentration, thus the only source of long-lead forecast skill is the land surface initial condition. When the trend is retained (Fig. 10c), statistically significant JJA T2m skill is found in all the three regions of interest, like in the GEM5.2-NEMO hindcast (Fig. 1g) and Exp 1 (Fig. 10a). For the interannual variability component, the detrended part (Fig. 10d), skillful JJA T2m forecasts are obtained in Regions 2 and 3, consistent with the GEM5.2-NEMO hindcast (Fig. 6g). In fact, the magnitude of correlation skill in Regions 2 and 3 of Exp 2 (Fig. 10d) is comparable to that of the GEM5.2-NEMO hindcast (Fig. 6g), indicating that the land surface initial condition contributes greatly to the interannual variability component of the long-lead forecast skill in these two regions.

Trends are introduced to Exp 1 through ocean and sea ice initial conditions and generated by radiative forcing due to changes in greenhouse gas concentrations during the 40-year hindcast period. In Exp 2, as the greenhouse gas concentration is fixed, trends originate only from initial conditions of land surface, including snow cover and soil moisture. The above analysis shows that the long-lead summertime forecast skill in Region 1 results mainly from the trend. In Regions 2 and 3, the forecast skill is associated with the interannual variability of the ocean and sea ice (Exp 1), and land surface (Exp 2), and is enhanced by the trend.

Next, we further investigate the processes that are responsible for the long-lead JJA forecast skill of the interannual variability in Regions 2 and 3. To assess the contribution of SST, area averaged detrended JJA T2m anomalies in Regions 2 and 3 are correlated with SST anomalies in March-April-May (MAM) for the observations and for the Exp 1 forecasts, which are shown in Fig. 11. The observed JJA T2m anomalies in Region 2 are not found to be strongly correlated with MAM SST (Fig, 11a), whereas in the Exp 1 forecast there are strong negative correlations in the tropical Pacific with a pattern similar to that of ENSO-correlated SST anomalies (Fig. 11b). This indicates that the model overestimates the Region 2 T2m response to SST anomalies, although the ensemble averaging may enhance the correlations by filtering out the noise. The lack of significant forecast skill of Exp 1 in Region 2 (Fig. 10b) is likely due to this disagreement between the model and observations. On the other hand, in Region 3, both the observed (Fig. 11c) and model forecast (Fig. 11d) JJA T2m anomalies are significantly correlated with MAM SST anomalies in the tropical eastern Pacific, i.e., a positive JJA T2m anomaly in the western US is associated with a La Nina-type tropical SST anomaly in MAM. This contributes to the skillful long-lead JJA forecast in Exp 1 for the interannual variability in Region 3 (Fig. 10b). Therefore, the ENSO-like SST anomaly in spring is an important source of forecast skill in JJA in the western United States region. It is a little surprising to note that cold SST off the coast of the western USA is associated with warm summers over the adjacent land area. This suggests that a La Nina SST is forcing a circulation anomaly, resulting in warm temperature over the land. The cold SST off the coast is likely just a response to the circulation anomaly and has little impact on the T2m over the land.

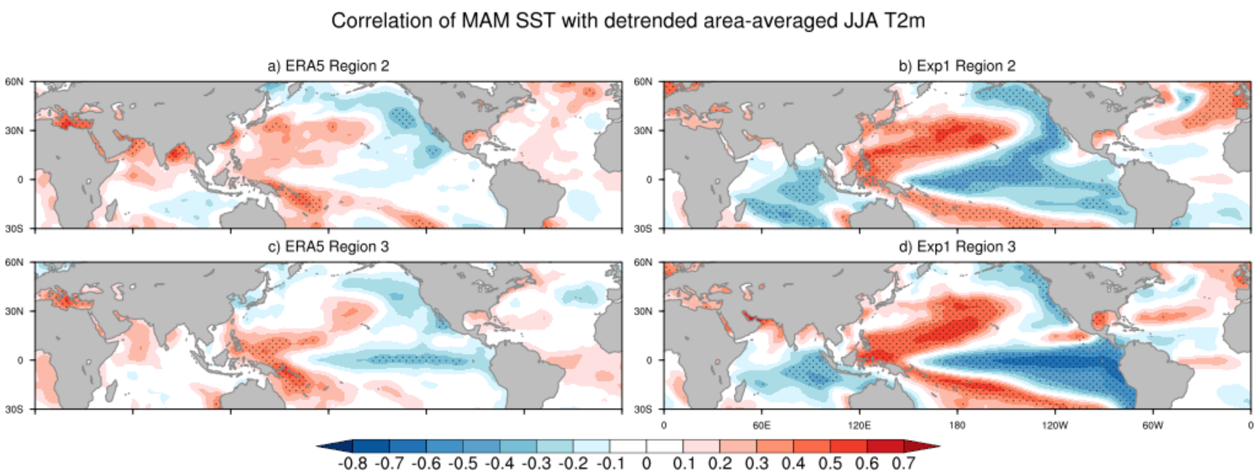

Figure 11 Correlation between observed MAM SST and area-averaged JJA T2m in (a) Region 2, and (c) Region 3; Correlation between Exp 1 forecast MAM SST and area-averaged JJA T2m in (b) Region 2, and (d) Region 3. The calculation is done for detrended anomalies. Stippling indicates that the correlation is statistically significant at the 0.05 level based on a Student's *t* test.

The contribution of land surface processes to the long-lead summertime forecast skill is assessed using the hindcast output of Exp 2. To answer the question of what land surface anomalies in the February 1 initial condition lead to summertime T2m anomalies in Regions 2 and 3, correlations are calculated between area averaged detrended JJA T2m anomalies in these two regions in Exp 2 and the snow amount, measured as snow water equivalent (SWE), and upper layer soil moisture in the February 1 initial condition, which is shown in Fig. 12. As can be seen, the JJA T2m anomalies in Region 2 and Region 3 are negatively correlated with the initial snow amount and soil moisture in the Siberian, and North American regions, respectively. The area-averaged snow amount and soil moisture are positively correlated at 0.48 and 0.55 in Regions 2 and 3, respectively, indicating that more (less) snow is associated with wetter (drier) soil. The correlation maps of Fig. 12 indicate that summertime predicted warm (cold) anomalies in these two regions can be traced back several months earlier to localized land surface conditions of below (above) normal snow amount and soil moisture.

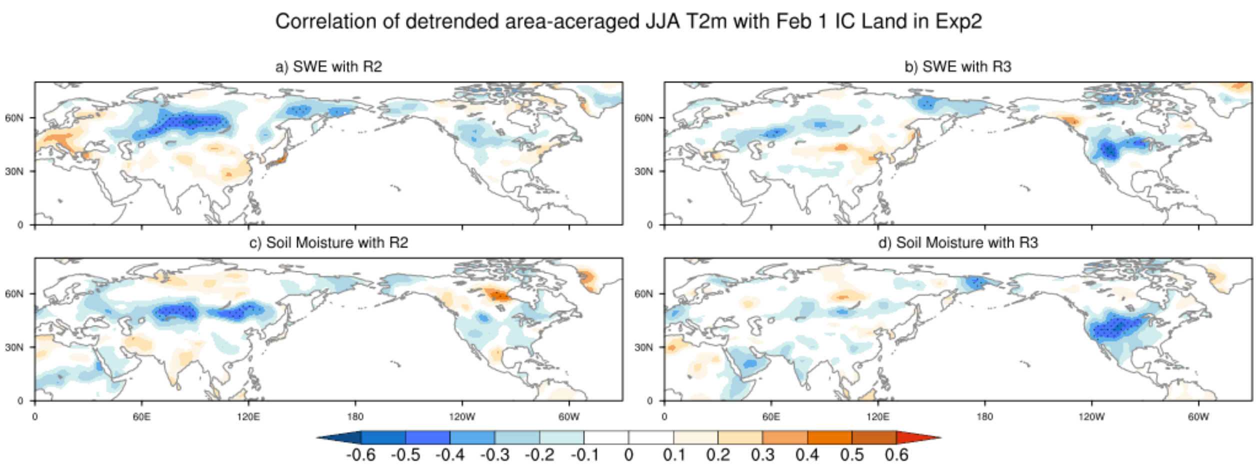

Figure 12 Correlation between February 1 (a and b) SWE, (c and d) upper layer soil moisture and Exp 2 forecast area averaged JJA T2m in Region 2 (left panels), and Region 3 (right panels). The calculation is done for detrended anomalies. Stippling indicates that the correlation is statistically significant at the 0.05 level based on a Student's *t* test.

Figure 13 shows the correlation between February 1 snow amount and seasonal mean T2m in MAM and JJA at each grid point in the observations and Exp 2 forecast. February 1 snow amount is negatively correlated with MAM T2m in the observations in the middle latitude Europe and North America (Fig. 13a). When it is correlated with JJA T2m, statistically significant negative correlations are seen over Regions 2 and 3 (Fig. 13b). Reduced (increased) winter snow amount in these two regions leads to localized warm (cold) summertime T2m anomalies. Similar associations of MAM and JJA T2m with winter snow amount are also observed in Exp 2 (Fig. 13c and d), although the model tends to overestimate this relationship compared to the observations. It is interesting to note that the impact of February 1 SWE on MAM T2m over the northern part of Region 2 is weak (Fig. 13a and c), when T2m is cold and the ground is covered with snow. The impact becomes strong in JJA (Fig. 13b and d) when the snow melts. Perhaps not surprisingly, an anomalously high (low) winter snow amount tends to lead to a longer (shorter) melting period and a cooler (warmer) summer. This suggests that anomalous winter snow amount over the Siberian and western United States regions has a delayed or long-lasting impact on the surface air temperature, which gives rise to the long-lead forecast skill.

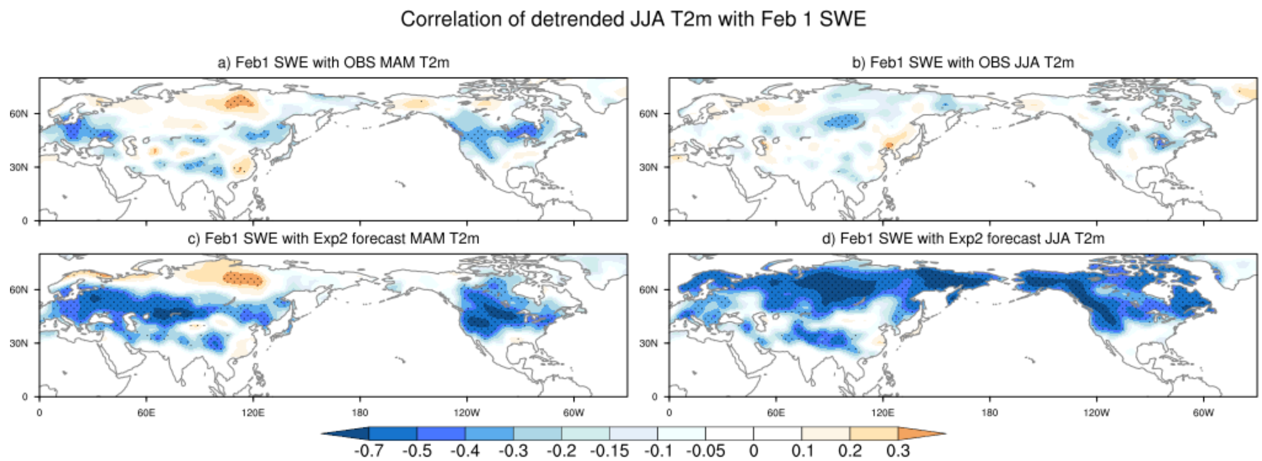

Figure 13 Temporal correlation between February 1 SWE and the ERA5 seasonal mean T2m in (a) MAM, and (b) JJA at each grid point. Correlation between February 1 SWE and the Exp 2 forecast seasonal mean T2m in (c) MAM, and (d) JJA. The calculations are calculated for detrended anomalies. Stippling indicates that the correlation is statistically significant at the 0.05 level based on a Student's *t* test.

7. Summary and discussion

In this study, we analyze the seasonal forecast skill based on 40-year hindcast output from two global coupled models in the CanSIPSv3 seasonal prediction system, with emphasis on the Northern Hemisphere middle latitude land areas in the summer season. The main findings are summarized below:

- Seasonal predictions for the summer season are skillful more than six months in advance in several Northern Hemisphere middle latitude land regions, including eastern Europe-Middle East (Region 1), Siberia-Mongolia-North China (Region 2), and the western Unites States (Region 3).
- The forecast skill of surface air temperature in these regions tends to peak in boreal summer seasons regardless of the lead time.
- Although a large part of the seasonal forecast skill of JJA T2m and Z500 in the Northern Hemisphere middle latitudes comes from the trend associated with global warming,

there is statistically significant long-lead seasonal forecast skill that is associated with the interannual variability, especially in Regions 2 and 3.

- The forecast skill centers tend to be connected to each other through an upper tropospheric circum-global teleconnection wave train.
- Several sources of predictability for the long-lead summertime seasonal forecast are identified from two idealized hindcast experiments using the GEM5.2-NEMO coupled model and its uncoupled atmospheric component. The trend is not only the main contributor to the skill in Region 1 (eastern Europe and Middle East), but also helps to enhance the forecast skill in Regions 2 and 3. An ENSO-like tropical SST anomaly is an important source of skill for the JJA season in the western United States (Region 3). Land surface conditions in winter, including snow amount and soil moisture, in the Siberian and western US regions have a delayed or long-lasting impact on the atmosphere, which leads to summer forecast skill of interannual variability in these regions.

Our analysis shows that JJA seasonal forecast skill benefits from trends. By looking at the 40-year JJA T2m trend in the ERA5 reanalysis (e.g., Fig. 14a; Fig. 1a of Teng et al. 2022), we can see that the observed trend itself has a distribution similar to the JJA forecast skill (Fig. 1) with positive centers in the Northern Hemisphere middle latitude land regions, collocated with Regions 1, 2 and 3. In the two CanSIPSv3 models, the forecast JJA T2m trend does not seem to depend on lead time. Both models produce warming trends in the middle latitude land regions. Figure 14 shows the forecast JJA T2m trend from the hindcasts initialized on February 1. The negative trend in the middle North Atlantic is likely associated with the problem of the ocean initial conditions of the Atlantic Meridional Overturning Circulation in the ORAS5 reanalysis, which is used in both CanSIPSv3 models, as is reported in Tietsche et al. (2020). GEM5.2-NEMO appears able to reproduce the distribution of the observations, with relatively large positive trend values in Regions 1, 2, and 3 (Fig. 14c). The amplitude of the trend at the centers in GEM5.2-NEMO, however, is underestimated. In CanESM5.1, the JJA T2m trend seems overestimated in the middle latitude land regions (Fig. 14e). A large part of the JJA T2m trend in GEM5.2-NEMO comes from the ocean and sea ice initial condition and GHG forcing (Fig. 14b). The warming over the Barents – Kara Seas area is likely associated with sea ice loss. The land surface initial condition contributes to the localized warming centers in Regions 1, 2 and 3 (Fig. 14d). By adding the trend in Exp 1 and Exp 2, Figure 14f shows that the contribution to the trend from the ocean and sea ice is largely independent of that from the land surface, as their sum is close to that of GEM5.2-NEMO hindcast (Fig. 14c). Improvement of trend representation in the models will likely further improve the JJA forecast skill in the Northern Hemisphere middle latitudes.

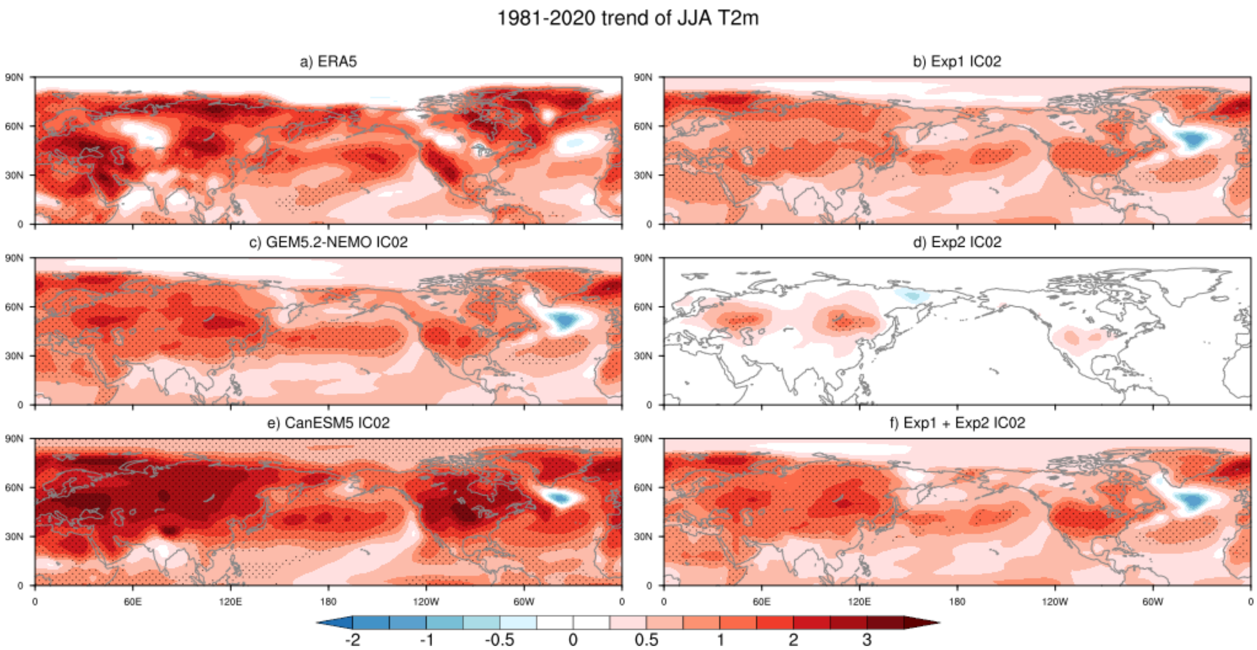

Figure 14 (a) JJA T2m trend in ERA5 reanalysis. JJA T2m trends from ensemble mean forecast obtained from 40-year hindcasts of (c) GEM5.2-NEMO, (e) CanESM5.1, (b) Exp 1, and (d) Exp 2. The hindcasts are initialized on February 1. (f) Sum of JJA T2m trend in Exp 1 and Exp 2. Unit: °C in 40 years. Stippling indicates that the linear trend is statistically significant at the 0.05 level based on a Student's *t* test.

The middle latitude regions of higher JJA forecast skill appear connected to each other and associated with a circum-global teleconnection (CGT) pattern. The CGT was observed in previous studies in the boreal summer associated with the trend and on the interannual time scale. The fluctuations of the Atlantic multi-decadal variability and the interdecadal Pacific oscillation were found to be correlated with the CGT (e.g., Teng et al. 2022). Teng and Branstator (2019) hypothesized that climate change can alter the basic circulation state and thereby enhance CGT as quasi-stationary Rossby waves by increasing their resonance. The CGT was found to be linked to forcing of the Indian summer monsoon (e.g., Ding and Wang 2005; Lin 2009), North American soil moisture (Teng et al. 2019), and Tibetan Plateau land temperature (Xue et al. 2022). From the current study, we show that the boreal summer CGT which is accompanied with the JJA forecast skill can be generated from ocean, sea ice and land surface initial conditions in the previous winter season. For example, as seen in Fig. 14d, trends from the winter land surface condition can result in a JJA T2m trend that resembles that associated with the CGT pattern. The winter land surface condition itself is likely influenced by climate change. How the sea ice loss contributes to the CGT trend is also of great interest. An improved understanding of the CGT dynamics is certainly helpful for seasonal predictions in the boreal summer.

A further interesting result from this study is that the land surface conditions, including snow amount and soil moisture, in winter or spring has a delayed or long-lasting impact on the JJA forecast skill in the middle latitude land regions. This implies that accurate land surface initial conditions and model representations of these land surface processes are crucial elements of seasonal forecasting systems and provide promising avenues for improving skill. Further studies are needed to better understand these processes and their contributions to predictability.

Acknowledgements

Members of the ECCC Seasonal Forum and many colleagues at RPN, CCCma, and CCMEP contributed to the development and implementation of CanSIPSv3. We thank the following colleagues for their various contributions to this project: Woo-Sung Lee, Slava Kharin, Paul Vaillancourt, Stéphane Chamberland, Michel Desgagné, Stéphane Bélair, Maria Abrahamowicz, Marco Carrera, Nicola Gasset, and Frederic Dupont.

Data Availability Statement

The CanSIPSv3 hindcast data used in this study are available for research upon reasonable request.

References

Becker, E., H. Van den Dool, and Q. Zhang, 2014: Predictability and forecast skill in NMME. *J. Climate*, 27, 5891–5906. https://doi.org/10.1175/JCLI-D-13-00597.1.

Beverley, J. D. , S. J. Woolnough , L. H. Baker , S. J. Johnson , and A. Weisheimer, 2019: The Northern Hemisphere circumglobal teleconnection in a seasonal forecast model and its relationship to European summer forecast skill. *Climate Dyn* ., 52, 3759–3771, https://doi.org/10.1007/s00382-018-4371-4.

Boer, G., 2009: Climate trends in a seasonal forecasting system. *Atmosphere–Ocean*, 47, 123–138. https://doi.org/10.3137/AO1002.2009.

Bradley, A. A., and S. S. Schwartz, 2011: Summary verification measures and their interpretation for ensemble forecasts. Mon. Wea. Rev., 139, 3075–3089, https://doi.org/10.1175/2010MWR3305.1.

Branstator, G. W., 2002: Circumglobal teleconnections, the jet stream waveguide, and the North Atlantic Oscillation. J Clim 15:1893–1910. https://doi.org/10.1175/1520-0442(2002)015%3c1893:CTTJSW%3e2.0.CO;2

Bretherton, C.S., M. Widmann, V.P. Dymnikov, J.M. Wallace, and I. Bladé, 1999: The effective number of spatial degrees of freedom of a time-varying field. *J. Clim.*, **12**, 1990-2009.

Butler, A. H., and Coauthors, 2016: The climate-system historical forecast project: Do stratosphere-resolving models make better seasonal climate predictions in boreal winter? *Quart. J. Roy. Meteor. Soc.*, 142, 1413–1427, https://doi.org/10.1002/qj.2743.

Carrera, M. L., S. Bélair, V. Fortin, B. Bilodeau, D. Charpentier, and I. Doré, 2010: Evaluation of snowpack simulations over the Canadian Rockies with an experimental hydrometeorological modeling system. *J. Hydrometeor.*, 11, 1123–1140, https://doi.org/10.1175/2010JHM1274.1.

Changnon, S., K. Kunkel, and B. Reinke, 1996: Impacts and responses to the 1995 heat wave: A call to action. *Bull. Amer. Meteor. Soc.*, 77, 1497–1506, https://doi.org/10.1175/1520-0477(1996)077,1497:IARTTH.2.0.CO;2.

Côté, J., S. Gravel, A. Méthot, A. Patoine, M. Roch, and A. Staniforth, 1998: The operational CMC-MRB Global Environmental Multiscale (GEM) model: Part I—Design considerations and formulation. *Mon. Wea. Rev.*, 126, 1373–1395, https://doi.org/10.1175/1520-0493(1998)126<1373:TOCMGE>2.0.CO;2.

Derome, J., G. Brunet, A. Plante, N. Gagnon, G. J. Boer, F. W. Zwiers, S. Lambert, and H. Ritchie, 2001: Seasonal predictions based on two dynamical models. Atmos.–Ocean, 39, 485–501. https://doi.org/10.1080/07055900.2001.9649690.

Ding, Q, and B. Wang, 2005: Circumglobal teleconnection in the Northern Hemisphere summer. J Clim 18:3483–3505. https://doi.org/10.1175/JCLI3473.1

Ding, Q, B. Wang, J. M. Wallace, and G. Branstator, 2011: Tropical-extratropical teleconnections in boreal summer: observed interannual variability. J Clim 24:1878–1896. https://doi.org/10.1175/2011JCLI3621.1.

Dirkson, A., W. J. Merryfield, and A. Monahan, 2017: Impacts of sea ice thickness initialization on seasonal Arctic sea ice predictions. *J. Climate,* 30, 1001–1017, https://doi.org/10.1175/JCLI-D-16-0437.1.

Doblas-Reyes, F.J., R. Hagedorn, T. N. Palmer, and J.-J. Morcrette, 2006: Impact of increasing greenhouse gas concentrations in seasonal ensemble forecasts. *Geophysical Research Letters*, 33, 1-5.

Fichefet, T., and M. A. Morales Maqueda, 1997. Sensitivity of a global sea ice model to the treatment of ice thermodynamics and dynamics. JGR, 102, 12609–12646.

Girard, C., and Coauthors, 2014: Staggered vertical discretization of the Canadian Environmental Multiscale (GEM) model using a coordinate of the log-hydrostatic-pressure type**.** *Mon. Wea. Rev.*, 142, 1183–1196, https://doi.org/10.1175/MWR-D-13-00255.1.

Hersbach, H., and Coauthors, 2020: The ERA5 global reanalysis. *Quart. J. Roy. Meteor. Soc.*, 146, 1999–2049, https://doi.org/10. 1002/qj.3803.

Jia, L., and Coauthors, 2022: Skillful seasonal prediction of North American summertime heat extremes, *J. Clim.*, **35**, 4331-4345. https://doi.org/10.1175/JCLI-D-21-0364.1.

Johnson, N. C., D. C. Collins, S. B. Feldstein, M. L. L'Heureux, and E. E. Riddle, 2014: Skillful wintertime North American temperature forecasts out to four weeks based on the state of ENSO and the MJO. Wea. Forecasting, 29, 23–38, https:// doi.org/10.1175/WAF-D-13-00102.1.

Kharin, V. V., Q. Teng, F. W. Zwiers, G. J. Boer, J. Derome, and J. S. Fontecilla, 2009: Skill assessment of seasonal hindcasts from the Canadian historical forecast project. *Atmos.–Ocean*, 47, 204–223, https://doi.org/10.3137/AO1101.2009.

Kharin, V. V., and J. F. Scinocca, 2012: The impact of model fidelity on seasonal predictive skill. *Geophys. Res. Lett.*, **39**, L18803, doi:10.1029/2012GL052815.

Kharin, V. V., W. J. Merryfield, G. J. Boer, and W.-S. Lee, 2017: A post-processing method for seasonal forecasts using temporally and spatially smoothed statistics. Mon. Wea. Rev., 145, 3545–3561, https://doi.org/10.1175/MWR-D-16-0337.1.

Kim, H.-M., P. J. Webster, and J. A. Curry, 2012: Seasonal prediction skill of ECMWF syetem 4 and NCEP CFSv2 retrospective forecast for the Northern Hemisphere winter. Climate Dyn., 39, 2957–2973, https://doi.org/10.1007/s00382-012-1364-6.

Krishnamurti, T. N., C. M. Kishtawal, T. E. LaRow, D. R. Bachiochi, Z. Zhang, C. E. Williford, S. Gadgil, and S. Surendran, 1999: Improved weather and seasonal climate forecasts from multimodel superensemble. *Science*, 285, 1548–1550, https://doi.org/10.1126/science.285.5433.1548.

Lin, H., 2009: Global extratropical response to diabatic heating variability of the Asian Summer Monsoon. J Atmos Sci 66:2697–2713. https://doi.org/10.1175/2009JAS3008.1.

Lin, H., R. Mo, and F. Vitart, 2022: The 2021 western North American heatwave and its subseasonal predictions. *Geophysical Research Letters, 49,* https://doi.org/10.1029/2021GL097036.

Lin, H., N. Gagnon, S. Beauregard, R. Muncaster, M. Markovic, B. Denis, and M. Charron, 2016: GEPS based monthly prediction at the Canadian Meteorological Centre. **Mon. Wea. Rev.**, 144, 4867–4883, https://doi.org/10.1175/MWR-D-16-0138.1.

Lin, H., and Coauthors, 2020: The Canadian Seasonal to Interannual Prediction Prediction System Version 2 (CanSIPSv2). *Wea. Forecasting*. 35, 1317–1343, https://doi.org/10.1175/WAF-D-19-0259.1.

Lin, H., and Coauthors, 2021: The Canadian Seasonal to Interannual Prediction System version 2.1 (CanSIPSv2.1). Environment and Climate Change Canada Tech. Note, 44 pp., https://iridl.ldeo.columbia.edu/documentation/Models/NMME/CanSIPS-IC3/technote.pdf.

Liniger, M.A., H. Mathis, C. Appenzeller, and F. J. Doblas-Reyes, 2007: Realistic greenhouse gas forcing and seasonal forecasts. *Geophysical Research Letters*, 34, 1–5.

Noilhan, J., and S. Planton, 1989: A simple parameterization of land surface processes for meteorological models. *Mon. Wea. Rev.*, 117, 536–549, https://doi.org/10.1175/1520-0493(1989)117<0536:ASPOLS>2.0.CO;2.

Noilhan, J., and J. F. Mahfouf, 1996: The ISBA land surface parameterisation scheme. *Global Planet. Change*, 13, 145–159, https://doi.org/10.1016/0921-8181(95)00043-7.

Peng, P., A. Kumar, and M. S. Halpert, 2012: An Analysis of CPC's Operational 0.5-Month Lead Seasonal Outlooks, Weather and Forecasting, 27, 898-917.

Scaife, A. A., and Coauthors, 2014: Skillful long-range prediction of European and North American winters. *Geophysical Research Letters*, 41, 2514–2519, https://doi.org/10.1002/2014GL059637.

Seneviratne, S. I., and Coauthors. 2012: Changes in climate extremes and their impacts on the natural physical environment. Managing the Risks of Extreme Events and Disasters to Advance Climate Change Adaptation, C. B. Field, Eds., Cambridge University Press. 109–230.

Shukla, J., and Coauthors, 2000: Dynamical seasonal prediction. *Bull. Amer. Meteor. Soc.*, **81**, 2593–2606, https://doi.org/10.1175/1520-0477(2000)081<2593:DSP >2.3.CO;2.

Sigmond, M., and Coauthors, 2023: Improvements in the Canadian Earth System Model (CanESM) through systematic model analysis: CanESM5.0 and CanESM5.1. *Geoscientific Model Development*, **16**. 6553-6591, https://doi.org/10.5194/gmd-16-6553-2023.

Sospedra-Alfonso, R., and Coauthors, 2024: Evaluation of Soil Moisture in the Canadian Seasonal to Interannual Prediction System, Version 2.1 (CanSIPSv2.1). *J. Appl. Meteorol. Climatol.*, **63**, 143-164. https://doi.org/10.1175/JAMC-D-23-0034.1.

Swart, N. C., and Coauthors, 2019: The Canadian Earth System Model version 5 (CanESM5.0.3). *Geosci. Model. Dev.* 12, 4823–4873. https://doi.org/10.5194/gmd-12-4823-2019.

Teng, H., G. Branstator, 2019: Amplification of waveguide teleconnections in the boreal summer, *Current Climate Change Reports*, 5. 421–432. https://doi.org/10.1007/s40641-019-00150-x.

Teng H, G. Branstator, A. B. Tawfik, and P. Callaghan, 2019: Circumglobal response to prescribed soil moisture over North America. J. Climate, 32,4525–4545, https://doi.org/10.1175/JCLI-D-18-0823.1.

Teng, H., R. Leung, G. Branstator, J. Lu, and Q. Ding, 2022: Warming Pattern over the Northern Hemisphere Midlatitudes in boreal summer 1979-2020. J. Climate, 35, 3479-3494. DOI: 10.1175/JCLI-D-21-0437.1

Tietsche, S., M. Balmaseda, H. Zuo, C. Roberts, M. Mayer, and L. Ferranti, 2020: The importance of North Atlantic Ocean transports for seasonal forecasts. *Clim. Dyn*., 55. 1995-2011. https://doi.org/10.1007/s00382-020-05364-6.

Titchner, H. A., and N. A. Rayner (2014), The Met Office Hadley Centre sea ice and sea surface temperature data set, version 2: 1. Sea ice concentrations, *J. Geophys. Res. Atmos., 119*, 2864-2889, doi: 10.1002/2013JD020316.

Tivy, A., S. E. L. Howell, B. Alt, S. McCourt, R. Chagnon, G. Crocker, T. Carrieres, and J. J. Yackel, 2011: Trends and variability in summer sea ice cover in the Canadian Arctic based on the Canadian Ice Service Digital Archive, 1960–2008 and 1968–2008**.** *J. Geophys. Res.*, 116, C03007, https://doi.org/10.1029/2009JC005855.

Verseghy, D. L., 2000: The Canadian Land Surface Scheme (CLASS): Its history and future. *Atmos.–Ocean*, 38, 1–13, https://doi.org/10.1080/07055900.2000.9649637.

Wallace, J. M. and D. S. Guztler, 1981: Teleconnections in the geopotential height field during the Northern Hemisphere winter. *Mon. Wea. Rev*., 109, 784-812.

Weisheimer, A., D. J. Befort, D. MacLeod, T. Palmer, C. O'Reilly, and K. Strømmen, 2020: Seasonal forecasts of the twentieth century. *Bull. Amer. Meteor. Soc*., https://doi.org/10.1175/BAMS-D-19-0019.1.

Wilks, 2011: Forecast verification. *Int. Geophy.*, 100, 301-394. https://doi.org/10.1016/B978-0-12-385022-5.00008-7

Xue, Y., and Coauthors, 2022: Spring land temperature in Tibetan Plateau and global-scale summer precipitation. *Bull. Amer. Meteor. Soc*., https://doi.org/10.1175/BAMS-D-21-0270.1.

Yeh, S.-W., and Coauthors, 2018: ENSO atmospheric teleconnections and their response to greenhouse gas forcing. *Rev. Geophys.*, **56**, 185–206, https://doi .org/10.1002/2017RG000568.

Zuo, H., Balmaseda, M. A. and Mogensen, K., 2015. The new eddy-permitting ORAP5 ocean reanalysis: description, evaluation and uncertainties in climate signals. Climate Dynamics, 10.1007/s00382-015-2675-1.